



Thermal expansion of CaIrO determined by X-ray powder diffraction

Alex Lindsay-Scott, Ian G. Wood, David P. Dobson

► To cite this version:

Alex Lindsay-Scott, Ian G. Wood, David P. Dobson. Thermal expansion of CaIrO determined by X-ray powder diffraction. *Physics of the Earth and Planetary Interiors*, 2007, 162 (1-2), pp.140. 10.1016/j.pepi.2007.04.003 . hal-00532105

HAL Id: hal-00532105

<https://hal.science/hal-00532105>

Submitted on 4 Nov 2010

HAL is a multi-disciplinary open access archive for the deposit and dissemination of scientific research documents, whether they are published or not. The documents may come from teaching and research institutions in France or abroad, or from public or private research centers.

L'archive ouverte pluridisciplinaire **HAL**, est destinée au dépôt et à la diffusion de documents scientifiques de niveau recherche, publiés ou non, émanant des établissements d'enseignement et de recherche français ou étrangers, des laboratoires publics ou privés.

Accepted Manuscript

Title: Thermal expansion of CaIrO_3 determined by X-ray powder diffraction

Authors: Alex Lindsay-Scott, Ian G. Wood, David P. Dobson

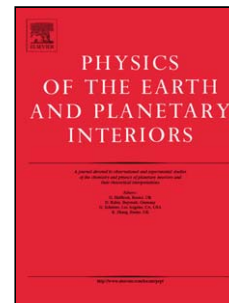
PII: S0031-9201(07)00063-5
DOI: doi:10.1016/j.pepi.2007.04.003
Reference: PEPI 4808

To appear in: *Physics of the Earth and Planetary Interiors*

Received date: 6-12-2006
Revised date: 22-3-2007
Accepted date: 3-4-2007

Please cite this article as: Lindsay-Scott, A., Wood, I.G., Dobson, D.P., Thermal expansion of CaIrO_3 determined by X-ray powder diffraction, *Physics of the Earth and Planetary Interiors* (2007), doi:10.1016/j.pepi.2007.04.003

This is a PDF file of an unedited manuscript that has been accepted for publication. As a service to our customers we are providing this early version of the manuscript. The manuscript will undergo copyediting, typesetting, and review of the resulting proof before it is published in its final form. Please note that during the production process errors may be discovered which could affect the content, and all legal disclaimers that apply to the journal pertain.



Thermal expansion of CaIrO_3 determined by X-ray powder diffraction

Alex Lindsay-Scott, Ian G. Wood and David P. Dobson*

Department of Earth Sciences, University College London, Gower Street, London,
WC1E 6BT, U.K.

* To whom all correspondence should be addressed: Email; d.dobson@ucl.ac.uk

Keywords: Post-Perovskite, CaIrO_3 , Thermal expansion, Grüneisen approximation, X-ray powder diffraction.

Abstract

The thermal expansion of CaIrO_3 , the archetype phase of the “post-perovskite” polymorph of MgSiO_3 , has been determined by X-ray powder diffraction from 113 K to 1173 K. For temperatures above 298 K, the volumetric coefficient of thermal expansion, $\alpha(T)$, can be represented by $\alpha(T) = a_0 + a_1(T)$, with $a_0 = 2.64(2) \times 10^{-5} \text{ K}^{-1}$ and $a_1 = 0.72(4) \times 10^{-8} \text{ K}^{-2}$. The data for the full range of temperature investigated can be fitted well by a second-order Grüneisen approximation to the zero-pressure volumetric equation of state, with the internal energy calculated *via* a Debye model, and parameters: $q_D = 703(11) \text{ K}$, $V_0 = 225.666(6) \text{ Å}^3$, $K'_0 = 4.8(4)$ and $(V_0 K_0 / g') = 2.77(2) \times 10^{-17} \text{ J}$, where q_D is the Debye temperature, V_0 is the unit-cell volume at $T = 0 \text{ K}$, K'_0 is the first derivative with respect to pressure of the incompressibility, K_0 , and g' is a Grüneisen parameter. The results of similar procedures, applied to the individual lattice parameters, suggest that the degree of elastic anisotropy shown by CaIrO_3 at ambient pressure may be much greater than that calculated for the high-pressure post-perovskite polymorph of MgSiO_3 .

1. Introduction

Until very recently, MgSiO_3 perovskite was thought to be the dominant phase throughout the Earth's lower mantle. However, the observation that perovskite-structured MgSiO_3 transforms to an orthorhombic CaIrO_3 -structured phase at around 120 GPa (Murakami *et al.*, 2004, Oganov and Ono, 2004) implies that a post-perovskite (CaIrO_3 -structured) MgSiO_3 phase (hereafter denoted post-perovskite) might be responsible for the D'' region at the base of the lower mantle. The physical and chemical properties of post-perovskite are therefore likely to dominate the dynamics of much of the core-mantle boundary region. Fig. 1 shows the CaIrO_3 post-perovskite type-structure with sheets of corner- and edge-sharing IrO_6 octahedra separated by Ca cation interlayers. This layered structure results in significantly higher shear-wave anisotropy in post-perovskite than in perovskite. The presence of a dominantly post-perovskite D'' layer is therefore consistent with regional variations in lower-mantle shear-wave anisotropy (see e.g. Hernlund *et al.*, 2005; Wookey *et al.* 2005).

The space group of the post-perovskite structure is $Cmcm$, with $Z = 4$. For CaIrO_3 , $a \sim 3.15 \text{ \AA}$, $b \sim 9.86 \text{ \AA}$, $c \sim 7.30 \text{ \AA}$ at room temperature (Rodi and Babel, 1965). The Ir ions lie on the $4a$ sites, with fractional coordinates 0, 0, 0; the Ca and O1 ions lie on the $4c$ sites at 0, y , $1/4$, with $y \sim 0.250$ and $y \sim 0.933$ respectively; the O2 ions lie on the $8f$ sites, at 0, y , z , with $y \sim 0.630$ and $z \sim 0.055$.

The very high pressures of stability of post-perovskite MgSiO_3 render precise measurements of its physical properties problematical. CaIrO_3 is the structural type phase of post-perovskite and is stable at ambient temperature and pressure. It is therefore studied experimentally as an isovalent, low-pressure analogue of post-perovskite (see e.g. Hirose and Fujita, 2005). Here we present measurements of the thermal expansion of CaIrO_3 over the temperature range from 113 K - 1173 K.

2. Experimental details

The sample of CaIrO_3 was prepared from a powder mixture of molar ratio 1:1.25 $\text{CaO}:\text{IrO}_2$ (it had been found, in previous syntheses, that metastable perovskite-structured CaIrO_3 persisted with Ca_2IrO_4 at Ca-excess, so excess IrO_2 was added to the starting mixture). Dry CaO (Alfa Aesar 99.998%) and IrO_2 (Alfa Aesar 99%) powders were ground together under acetone and pelleted prior to sintering in air for 45 hours at 1273 K. The recovered pellet was then re-ground, pelleted and further sintered at 1348 K for 70 hours. X-ray powder diffraction of part of this sample then showed that reaction was complete, with only orthorhombic (Cmcm) CaIrO_3 and minor amounts of IrO_2 and Ir present.

To investigate the thermal expansion, X-ray powder diffraction data were collected using a PANalytical X'Pert Pro diffractometer, with Bragg-Brentano parafocusing reflection geometry. This instrument is equipped with a $\text{Ge}(111)$ Johansson geometry focusing monochromator, producing a $\text{Co K}\alpha_1$ incident beam, the wavelength of which was assumed to be 1.788996 Å (Hölzer *et al.*, 1997). The X-ray tube was operated at 40 kV and 30 mA. In the incident- and diffracted-beam optics, variable-width divergence and anti-scatter slits were used, together with a 10 mm wide beam mask in the incident beam, so as to illuminate a constant 10 mm x 10 mm area of the sample; 0.04 radian Soller slits were present in both the incident and diffracted beams to reduce the axial divergences. The X-ray detector was an “X'Celerator” position-sensitive detector; this device covers an angular range in 2θ of $\pm 1.061^\circ$, with an effective fixed step size of 0.0167° . Data were collected over the 2θ range from 18.5 to 143.9° , with a data collection time of 50 minutes.

Diffraction data between 113 K and 283 K were obtained using an Anton Paar TTK 450 low-temperature stage cooled by liquid N_2 , and data between 298 K and 1173 K were collected using an Anton Paar HTK1200N heated stage. The samples used consisted of

80.1 wt % of MgO (Aldrich 99.99%) mixed with the CaIrO_3 ; the purpose of the MgO was to aid in reducing preferred orientation in the CaIrO_3 and to help to constrain determination of the specimen displacement, transparency, and 2θ offset in the Rietveld refinements.

X-ray diffraction measurements were made at intervals of 10 or 20 K between 113 and 333 K and at intervals of 20 K between 333 and 1173 K. Measurements below 298 K were taken under a vacuum of ~ 5 mbar and above 298 K in air. At each temperature increment above 298 K, the sample was heated at 5 K per minute after which it was equilibrated for a time which varied from 25 minutes at 323 K to 6 minutes at 413 K and above. Below 298 K, temperatures were changed manually and the sample was then allowed to equilibrate for at least 25 minutes before the diffraction patterns were measured. The temperature control was to better than ± 0.5 K throughout; however, in our first heating run of the sample it was found that, due to a malfunction of the temperature-control system, there were much larger temperature fluctuations in the interval $693 \text{ K} \leq T \leq 1033 \text{ K}$. After correcting the fault, this section of the high-temperature experiment was, therefore, repeated; any systematic offset between the two high-temperature experiments was judged to be negligible.

The intensities of the diffraction data were converted from variable to fixed divergence slit geometry using software supplied by the manufacturer, after which the data were analysed by Rietveld refinement using the GSAS suite of programmes (Larson and Von Dreele, 2000; Toby, 2001). The CaIrO_3 sample was found to be highly textured and so an empirical 12th-order spherical-harmonic preferred orientation correction was applied to this phase; the texture indices were found to be 4.1 for the sample used above room temperature and 2.3 for the sample used below room temperature. In addition to the cell parameters, the fractional coordinates of the atoms in the CaIrO_3 phase were refined, as were isotropic atomic displacement parameters, constrained such that those for O1 and

O₂ were equal and that for Ca was 3x that for Ir (after Rodi and Babel, 1965). Four phases (MgO, CaIrO₃, Ir, IrO₂) were included in the refinement above 298 K; below 273 K, it was necessary to include also ice Ih (this was done using the Le Bail method as the film of ice deposited on the sample was too strongly textured for successful Rietveld refinement). As the sample is heated (or cooled) small changes in the position of the sample in the diffractometer will occur. If accurate cell parameters are to be obtained, it is essential, therefore, to include the specimen displacement as a variable parameter in the refinement; for this to be done successfully requires data to be collected over the widest possible range of 2θ . It is also highly desirable to mix a cubic calibrant (in this case MgO) with the sample; refinement of the cell parameter of this calibrant, together with the positional aberrations of the diffractometer, strongly constrains the exact geometry of the instrument at each temperature. In total, fifty variables were included in the refinement with 7,375 data points. The mean χ^2 was 1.50 for 298 K - 1173 K and 3.3 for 113K - 283 K; the weighted profile R-factors (background subtracted) were typically 0.19 throughout. For one of the low temperature data sets (263 K), free refinement of the MgO and CaIrO₃ lattice parameters gave values that differed significantly from the expected smooth variation; for this one data set the cell parameter of the MgO was, therefore, not varied but fixed at a value interpolated from adjacent data points. Examples of diffraction patterns, collected at room temperature and 1173 K are presented in Fig. 2.

Prior to our study of CaIrO₃, calibration experiments were carried out in which the cell parameters of Si (NBS: SRM640) mixed with MgO (Aldrich, 99.99%) were determined between 298 K and 1273 K by the method described above. Our refined value for the cell parameter of the SRM640 Si at 298 K agreed with the published value (Yoder-Short 1993) to 0.000019 Å (or 0.6 standard uncertainties) and our values for the linear thermal expansion of the Si, to 1273 K, agreed with laser interferometer measurements

(Watanabe *et al.* 2004, White and Mingos 1997) always to better than 0.01%. Similarly, our measurements, to 1173 K, of the thermal expansion of the MgO calibrant, when mixed with the CaIrO_3 sample, agreed very well with previous dilatometer measurements (Suzuki 1975). For temperatures above 298 K, we found that our values for the MgO cell volume could be brought into effectively exact coincidence with those of Suzuki (1975) by a linear correction to the temperature of zero at 298 K and +8 K at 1173 K; below room temperature, our values were also in excellent agreement with Suzuki's extrapolated dilatometer values (note, however, that no temperature correction has been applied to the results reported here as, in view of the excellent agreement we had obtained for the Si data, there is no *a priori* reason to suppose that the discrepancy was due to errors in the present measurements). We, therefore, have confidence that our results for CaIrO_3 are accurate.

3. Results and discussion

3.1. Thermal expansion

The observed unit cell parameters for CaIrO_3 as a function of temperature are shown in Table 1; they are consistent with the values (at ambient temperature) from previous single-crystal and powder diffraction studies of this material, though of somewhat higher precision. Fig. 3 shows the variation of the cell parameters and volume between 113 and 1173 K; it can be seen that the thermal expansion is strongly anisotropic, being greatest for the b -axis (i.e. for the direction perpendicular to the sheets of IrO_6 octahedra and Ca ion interlayers) and smallest for the a -axis (i.e. along the chains of edge-sharing IrO_6 octahedra).

Since it is probably the properties of CaIrO_3 at high temperatures that will be of most interest to earth scientists, we obtained linear and volumetric thermal expansion values in the form tabulated by Fei (1995) by fitting the data from 298 K to 1173 K to

$$V(T) = V_{Tr} \exp \left[\int_{Tr}^T \mathbf{a}(T) dT \right] \quad (1)$$

where V_{Tr} is the volume at a chosen reference temperature, Tr , (here taken to be 300 K) and $\mathbf{a}(T)$ is the volumetric thermal expansion coefficient, having the form

$$\mathbf{a}(T) = a_0 + a_1 T \quad (2)$$

The resulting values of V_{Tr} , a_0 and a_1 are shown in Table 2, together with the results of similar fits to obtain the linear thermal expansion coefficients of the three axes of the unit cell.

A more physically meaningful interpretation of the thermal expansion curve, encompassing its full temperature range, can be obtained using Grüneisen approximations for the zero-pressure equation of state (see e.g. Wallace, 1998), which also allow estimates of the Debye temperature of the material to be made. For data covering a wide temperature range, the second-order Grüneisen approximation is more appropriate than the first-order approximation (Vocadlo *et al.*, 2002). This approximation, derived on the basis of a Taylor series expansion of (PV) to second-order in DV (for details, see Wallace, 1998), takes the form

$$V(T) = V_0 U / (Q - bU) + V_0 \quad (3)$$

where $Q = V_0 K_0 / g'$ and $b = (K_0' - 1) / 2$; g' is a Grüneisen parameter (assumed constant) K_0 and K_0' are the incompressibility and its first derivative with respect to pressure, respectively, at $T = 0$ K, and V_0 is the volume at $T = 0$ K. The internal energy, U , may be calculated as a function of temperature using the Debye approximation (see e.g. Poirier 2000) from

$$U(T) = 9Nk_B T (T/q_D)^3 \int_0^{q_D/T} x^3 / (\exp(x) - 1) dx \quad (4)$$

where k_B is Boltzmann's constant and q_D is the Debye temperature; since we are using equation (3) to fit the unit-cell volume, N is the number of atoms in the unit cell.

The solid line in Fig. 3d shows the result obtained from fitting the data for $V(T)$ to equation (3) by weighted non-linear least-squares; Table 3 lists the values of the four fitted parameters. It can be seen from the Figure that this model provides an excellent description of the behaviour of the cell volume over the full temperature range of the experiment. This point is further illustrated in Fig. 4, which shows the behaviour of the resulting volumetric thermal expansion coefficient $\alpha(T)$ obtained from

$$\alpha(T) = (1/V)(dV/dT) \quad (5)$$

The full line in Fig. 4 gives the result obtained by differentiation of equation (3), while the points show the results from simple numerical differentiation by differences of the $V(T)$ data. Again, it can be seen that the agreement is very good, despite the deficiencies of the theory. In particular, the neglect of anharmonicity can lead to an underestimate of the thermal expansion coefficient at high temperatures (see e.g. Wood *et al.* 2002), but there is little indication of this in the present case.

An estimate of the first pressure derivative of the incompressibility, K'_0 , may be obtained directly from the coefficient b in Eq. (3) and the resulting value, $K'_0 = 4.8(4)$, seems very reasonable. Estimates of the incompressibility, K_0 , cannot be obtained *via* Eq. (3) unless the Grüneisen parameter, g , is known, which is not the case for CaIrO_3 . However, for the post-perovskite phase of MgSiO_3 , Tsuchiya *et al.* (2005), using density–functional perturbation theory, have calculated that the thermodynamic Grüneisen parameter, g , lies in the range from 1.14 to 1.2 at a pressure of 125 GPa and temperatures in the range from 300 K to 4000 K (i.e. within the stability field of MgSiO_3 post-perovskite). If we apply their mean value of $g(1.17)$ in the present case, we obtain a value of $K_0 = 144(1)$ GPa for CaIrO_3 , which once again would seem reasonable, though possibly a little low, perhaps suggesting that the value of g in CaIrO_3 is higher. However, although equation (3) provides a useful framework within which to

assess the behaviour of materials such as CaIrO_3 , the theory is deficient in several aspects; in particular, it is dependent on the validity of the Debye approximation, which has, for example, been shown in some respects to work rather poorly for perovskites (Oganov *et al.* 2000). These deficiencies in the model will be reflected in the fitted values of the parameters, which should therefore be interpreted with some caution.

A modification of this Grüneisen approximation, developed by Wachtman *et al.* (1962), has been applied successfully to model anisotropic linear expansion in materials such as olivines (Suzuki, 1975; Okajima *et al.*, 1978) (note, however, that, though leading to an equation of the correct functional form, the derivation given by Wachtman *et al.* (1962), is invalid since it conflates quantities of first-order and second-order smallness). Following a procedure similar to that described in Wallace (1998), but applying it to the unit-cell axes of a cubic crystal rather than to its volume, the following expression (to second order) for the behaviour of the a -axis may be obtained

$$a(T) = a_0 U / (Q_A - b_A U) + a_0 \quad (6)$$

where $Q_A = \mathbf{k}_{a0} V_0 / \mathbf{g}'$ and $b_A = (\mathbf{k}_{a0}' - 5)/2$. Here, the subscript “A” has been added to the coefficients Q and b to indicate that that we are considering axial rather than volumetric expansion; \mathbf{k}_{a0} is the axial incompressibility (i.e. $\mathbf{k}_a = -adP/da$) and \mathbf{k}_{a0}' is its first derivative with respect to pressure, evaluated at $T = 0$ K; \mathbf{g}' is a Grüneisen parameter and a_0 is the value of the a -axis at $T = 0$ K. For an orthorhombic crystal, equations of the form given in Eq. (6) obtain for each of the three axes of the unit cell, but the expression for the parameter b_A becomes a little more complex. Taking as an exemplar the a -axis of the orthorhombic crystal, then $Q_A = \mathbf{k}_{a0} V_0 / \mathbf{g}'$ (as before) and $b_A = [\mathbf{k}_{a0}' - 2(\mathbf{k}_{a0}/\mathbf{k}_{b0}) - 2(\mathbf{k}_{a0}/\mathbf{k}_{c0}) - 1]/2$; similar expressions apply to the b and c axes. The axial incompressibilities are related to the elastic compliances, s_{ij} , such that, for example, $\mathbf{k}_a = 1/(s_{11} + s_{12} + s_{13})$.

Equation (6) has been used to fit the data for $a(T)$, $b(T)$ and $c(T)$ and these results are also shown as solid lines in Fig. 3; Table 3 lists the values of the four fitted parameters in each case. Once again, it can be seen from the Figure that this model provides an excellent description of the behaviour of the individual cell parameters over the full temperature range of the experiment.

Using the values shown in Table 3, and assuming that the mean value of $g(1.17)$ applies in all cases, we obtain axial incompressibilities of 710(17) GPa, 327(3) GPa and 379(4) GPa for the a -, b - and c -axes respectively (note that these axial values will in general be of order three times greater than their volumetric equivalent). For an orthorhombic crystal, the bulk incompressibility, K_0 , should be equal to $1/(1/k_a + 1/k_b + 1/k_c)$; by combining the axial incompressibilities listed above in this way we obtain a value of 141(1) GPa for K_0 , in excellent agreement with that, 144(1) GPa, obtained by fitting the $V(T)$ data.

It is interesting also to compare these results for axial incompressibility with those derived from the elastic constants of the post-perovskite polymorphs of MgSiO_3 and Al_2O_3 , obtained *via* computer simulations by Stackhouse *et al.* (2005ab). Table 4 shows our axial incompressibility ratios for CaIrO_3 , together with those for MgSiO_3 and Al_2O_3 at 136 GPa and 0 K and 4000 K. It can be seen from the Table that, if correct, our results imply that there is a very much greater degree of elastic anisotropy in CaIrO_3 than in either MgSiO_3 or Al_2O_3 . In particular, it would seem that, relative to the other two directions, there is a much greater rigidity in CaIrO_3 along the line of the edge-sharing chains of IrO_6 octahedra than is found in MgSiO_3 or Al_2O_3 . This is, perhaps, not entirely surprising as in CaIrO_3 , which is stable at ambient pressure, compression along the b - and c -axes can be achieved by reduction in the layer separation and rotation of the corner-linked octahedra respectively. In the more densely packed, high-pressure polymorphs of MgSiO_3 or Al_2O_3 , there is less scope for these mechanisms to operate,

leading to a more isotropic behaviour. If this interpretation is correct it would imply that, on compression, CaIrO_3 would be expected to stiffen more rapidly along the b - and c -axes than along the a -axis. A further implication is that it seems likely that, in some important respects, the properties of CaIrO_3 at ambient pressure may provide a very imperfect analogue for the post-perovskite phase of MgSiO_3 . It is, however, of interest to note that this conclusion with regard to the rate of stiffening of the three axes is not supported by the values of the b_A parameters listed in Table 3, which lead to values for the pressure derivatives of the axial incompressibilities, k_{a0}' , k_{b0}' and k_{c0}' , of 51(6), -0.6(11) and 13(1) respectively (note that these axial values will, once again, be of order three times greater than their volumetric equivalent). Their mean value, 21(2), equivalent in volumetric terms to $K_0' = 7.0(7)$, is in fair agreement with that obtained previously by fitting the cell volume (4.8(4)), but their form, with k_{a0}' taking the largest value and k_{b0}' the smallest value is the opposite of that which is expected on the basis of the argument above. We consider that this apparent contradiction probably results from the deficiencies of the theory; the b parameters appear in Eq. (3) and Eq. (6) *via* the second-order terms (e.g. *via* $(DV)^2$) in the model and are thus far more sensitive to its defects (such as the neglect of the temperature dependence of the incompressibility) than are the Q parameters, which are introduced *via* the first-order terms (e.g. *via* (DV)).

The Debye temperatures resulting from fitting the three unit-cell axes correspond very well with that obtained from the unit-cell volume, their average value, 718(14) K, showing no significant difference from that, 703(11) K, obtained by fitting $V(T)$. The Debye temperatures for the a - and b -axes, 648(37) K and 647(15) K are very similar, with that for the c -axis, 859(13) K, significantly higher. Once again, it is of interest to compare this result with those obtained for MgSiO_3 by computer simulation. The similarity of q_D for the a - and b -axes and the higher q_D for the c -axis in CaIrO_3 would seem to be in accordance with the calculated phonon dispersion curves of

Tsuchiya *et al.* (2005) for post-perovskite MgSiO_3 at 120 GPa, which indicate higher frequencies for phonons travelling parallel to c^* .

3.2. Crystal Structure

X-ray powder diffraction provides a very suitable method for the determination of the unit-cell parameters of CaIrO_3 . However, the scattering by the oxygen ions is very weak relative to that from the Ir ions and so accurate determination of the oxygen fractional coordinates by this method is difficult to achieve; in addition, our samples showed strong preferred orientation and some of the low-temperature data sets also included peaks from very strongly oriented ice. Thus, although the fractional coordinates of the Ca, O1 and O2 ions were allowed to vary in the Rietveld refinements, we do not consider the resulting values to be very reliable. At 298 K, we have very good agreement with the single-crystal determination of Rodi and Babel (1965) for the Ca ion coordinate, with $y = 0.250(1)$ (compared with 0.2498). For the oxygen ions the agreement is much poorer; for O1 we have $y = 0.904(4)$ (c.f. 0.9331) and for O2 we have $y = 0.615(2)$ (c.f. 0.6296) and $z = 0.044(2)$ (c.f. 0.0553). The atomic displacement parameters from our refinement are also approximately twice as large as those reported by Rodi and Babel (1965); again, this probably reflects the influence of the preferred orientation of the sample. Similarly, the bond-angle variance of the IrO_6 octahedron is over three times larger than that reported previously, which suggests to us that it is our structure that is the less accurate of the two.

Our refinements do, however, serve to indicate that the change in structure between 300 K and 1173K is almost nil. Across this temperature range we found that: the position of the Ca ion was effectively invariant (any shift being orders of magnitude less than the standard uncertainty in this coordinate); the O1 y coordinate decreased by ~ 0.013 (~ 3 standard uncertainties); the O2 y and z coordinates increased by ~ 0.010 and ~ 0.005 (5

and 2.5 standard uncertainties respectively). In view of the expected limitations of the use of X-ray powder data with this material, we do not regard any of these shifts as significant.

Acknowledgements

We wish to thank Lidunka Vocadlo for assistance with the data analysis and for helpful discussions. DD gratefully acknowledges receipt of a Royal Society University research Fellowship. Funding for the X-ray powder diffractometer used in this study was provided by the U.K. Strategic Research Infrastructure Fund (SRIFII).

References

- Fei, Y. (1995) AGU Reference Shelf 2: Mineral Physics and Crystallography – A Handbook of Physical Constants, edited by T.J. Ahrens, pp 29-44. AGU, Washington
- Hernlund J.W., Thomas C. and Tackley P.J. (2005) A doubling of the post-perovskite phase boundary and structure of the Earth's lowermost mantle. *Nature*, **434**, 882-886
- Hirose K. and Fujita Y. (2005) Clapeyron slope of the post-perovskite phase transition in CaIrO_3 . *Geophysical Research Letters*, **32**, L13313, doi:10.1029/2005GL023219.
- Hölzer G., Fritsch M., Deutsch M., Härtwig J. and Förster E. (1997) $Ka_{1,2}$ and $Kb_{1,3}$ emission lines of the 3d transition metals. *Phys. Rev. A*, **56**, 4554-4568.
- Larson A.C. and Von Dreele R.B. (2000) "General Structure Analysis System (GSAS)", Los Alamos National Laboratory Report LAUR 86-748.
- McDaniel C.L. and Schneider S.J. (1972) Phase relations in the $\text{CaO-IrO}_2\text{-Ir}$ system in air. *J. Solid State Chemistry*, **4**, 275-280
- Murakami, M., Hirose, K., Kawamora, K., Sata, N., Ohishi, Y. (2004) Post Perovskite Phase Transition in MgSiO_3 . *Science*, **304**, 855-858.
- Oganov, A.R., Brodholt, J.P. and Price, G.D. (2000) Comparative study of quasi-harmonic lattice dynamics, molecular dynamics and Debye model applied to MgSiO_3 perovskite. *Phys. Earth Planet. Inter.* **122**, 277-288
- Oganov, A.R. and Ono S. (2004) Theoretical and Experimental Evidence for a Post-Perovskite Phase of MgSiO_3 in Earth's D'' layer. *Nature*, **430**, 445-448.
- Okajima S., Suzuki I., Seya K., Sumino Y. (1978) Thermal Expansion of Single-Crystal Tephroite. *Phys. Chem. Minerals* **3**, 111-115.
- Poirier J-P. (2000) Introduction to the physics of the Earth's interior (2nd ed.), Cambridge University Press, Cambridge, United Kingdom
- Rodi F. and Babel D. (1965) Erdalkaliiridium (IV)-oxide: Kristallstruktur von CaIrO_3 . *Z. Anorg. Allg. Chem.*, **336**, 17-23
- Stackhouse S., Brodholt J.P., Wookey J., Kendall J.-M. and Price G.D. (2005a) The effect of temperature on the seismic anisotropy of the perovskite and post-perovskite polymorphs of MgSiO_3 . *Earth and Plan. Sci. Lett.* **230**, 1-10.
- Stackhouse S., Brodholt J.P. and Price G.D. (2005b) High temperature elastic anisotropy of the perovskite and post-perovskite polymorphs of Al_2O_3 . *Geophys. Res. Lett.* **32**, L13305, doi:10.1029/2005GL023163.
- Suzuki I. (1975) Thermal expansion of periclase and olivine, and their anharmonic properties. *J. Phys. Earth*, **23**, 145-159
- Toby B.H. (2001) EXPGUI, a graphical user interface for GSAS. *J. Appl. Cryst.* **34**, 210-221

Tsuchiya J., Tsuchiya T. and Wentzcovitch R. M. (2005) Vibrational and thermodynamic properties of MgSiO_3 postperovskite. *J Geophys. Res.* **110**, B02204, doi:10.1029/2004/B003409.

Vocadlo, L., Knight, K.S., Price, G.D. & Wood, I.G. (2002). Thermal expansion and crystal structure of FeSi between 4 and 1173 K determined by time-of-flight neutron powder diffraction. *Phys. Chem. Miner.* **29**: 132-139

Wallace, D.C. (1998) *Thermodynamics of crystals*, Dover, New York

Watanabe H., Yamada N. and Okaji M. (2004) Linear thermal expansion coefficient of silicon from 293 to 1000 K. *International Journal of Thermophysics*, **25**, 221-236

Wachtman J.B., Scuderi T.G. & Cleek G.W. (1962) Linear thermal expansion of aluminium oxide and thorium oxide from 100 to 1000 K. *J Amer. Ceramic Soc.*, **45**, 319-323.

White G.K. and Minges M.L. (1997) Thermophysical properties of some key solids: an update. *International Journal of Thermophysics*, **18**, 1269-1327

Wood, I.G., Knight, K.S., Price, G.D. and Stuart, J.D. (2002) Thermal expansion and atomic displacement parameters of cubic KMgF_3 perovskite determined by high-resolution neutron powder diffraction. *J. Appl. Cryst.*, **35**, 291-295

Wookey J., Stackhouse S., Kendall J-M., Brodholt J. and Price G.D. (2005) Efficacy of the post-perovskite phase as an explanation for lowermost-mantle seismic properties. *Nature*, **438**, 1004-1007

Yoder-Short D. (1993) On a small error in SRM640, SRM640a and SRM640b lattice parameters. *J. Appl. Cryst.*, **26**, 272-276.

Figure Captions

Figure 1: The “post-perovskite” structure of CaIrO_3 , viewed along $[100]$, with sheets of corner- and edge-linked IrO_6 octahedra lying in the a - c plane separated by interlayers of Ca ions

Figure 2: Observed (points), calculated (line) and difference (lower trace) X-ray powder diffraction patterns for CaIrO_3 at 298 K (A) and 1173 K (B). The y-axis scale for $80 < 2\theta < 145^\circ$ has been enlarged for clarity. The tick marks show the positions of the Bragg reflections from (bottom up): MgO , CaIrO_3 , Ir and IrO_2 .

Figure 3: CaIrO_3 cell parameters and volume between 113 K and 1173 K. Experimental values are shown as points (error bars are smaller than the symbols used). The full lines show the fit of the data to a second-order Grüneisen approximation to the zero-pressure equation of state (see text for details).

Figure 4: CaIrO_3 : volumetric thermal expansion coefficient as a function of temperature. The points were obtained by numerical differentiation of the data shown in Fig 3; the solid line was obtained *via* equation (3).

Table 1: CaIrO₃ unit-cell parameters (values in parentheses are estimated standard uncertainties and refer to the least-significant digits).

T (K)	<i>a</i> (Å)	<i>b</i> (Å)	<i>c</i> (Å)
113	3.14332(7)	9.84958(15)	7.29008(10)
123	3.14338(7)	9.85003(15)	7.29040(10)
143	3.14344(9)	9.85098(18)	7.29082(12)
163	3.14374(8)	9.85198(21)	7.29149(13)
173	3.14396(7)	9.85323(16)	7.29177(10)
183	3.14393(7)	9.85428(15)	7.29215(10)
203	3.14411(7)	9.85586(16)	7.29299(10)
223	3.14443(7)	9.85748(16)	7.29407(11)
243	3.14468(8)	9.85913(15)	7.29491(11)
263	3.14499(8)	9.85983(17)	7.29592(12)
283	3.14529(8)	9.86293(18)	7.29700(12)
298	3.14572(7)	9.86403(14)	7.29753(9)
323	3.14610(7)	9.86651(14)	7.29894(9)
333	3.14623(7)	9.86752(13)	7.29951(9)
353	3.14651(7)	9.86985(13)	7.30065(8)
373	3.14677(7)	9.87215(15)	7.30205(9)
393	3.14711(7)	9.87443(14)	7.30340(9)
413	3.14751(7)	9.87660(14)	7.30471(9)
433	3.14786(7)	9.87908(13)	7.30603(9)
453	3.14826(7)	9.88111(13)	7.30737(8)
473	3.14847(7)	9.88349(14)	7.30891(9)
493	3.14888(7)	9.88598(13)	7.31021(9)
513	3.14927(7)	9.88841(14)	7.31185(9)
533	3.14965(7)	9.89060(14)	7.31342(9)
553	3.14988(7)	9.89319(13)	7.31481(9)
573	3.15039(7)	9.89536(14)	7.31644(9)
593	3.15082(7)	9.89816(14)	7.31792(9)
613	3.15104(7)	9.90024(13)	7.31951(9)
633	3.15156(7)	9.90292(13)	7.32100(9)
653	3.15188(7)	9.90521(14)	7.32246(9)
673	3.15247(7)	9.90758(14)	7.32414(9)
693	3.15287(6)	9.90966(12)	7.32564(8)
713	3.15331(7)	9.91197(13)	7.32729(8)
733	3.15374(6)	9.91434(13)	7.32904(8)
753	3.15409(7)	9.91669(13)	7.33059(8)
773	3.15458(6)	9.91945(13)	7.33216(8)
793	3.15494(7)	9.92167(13)	7.33393(8)
813	3.15553(6)	9.92427(13)	7.33559(8)
833	3.15587(6)	9.92664(13)	7.33726(8)
853	3.15640(7)	9.92896(13)	7.33899(9)
873	3.15678(6)	9.93191(13)	7.34075(8)
893	3.15725(7)	9.93407(13)	7.34234(9)
913	3.15765(7)	9.93633(13)	7.34395(9)
933	3.15808(6)	9.93880(13)	7.34566(8)
953	3.15860(6)	9.94101(13)	7.34734(9)
973	3.15890(7)	9.94353(13)	7.34901(9)

993	3.15941(7)	9.94592(13)	7.35065(9)
1013	3.16002(7)	9.94819(13)	7.35248(9)
1033	3.16043(7)	9.95101(13)	7.35417(9)
1053	3.16072(7)	9.95324(14)	7.35583(9)
1073	3.16139(7)	9.95583(14)	7.35750(9)
1093	3.16175(7)	9.95821(14)	7.35936(9)
1113	3.16217(7)	9.96070(14)	7.36102(9)
1133	3.16271(7)	9.96306(14)	7.36273(9)
1153	3.16301(7)	9.96562(13)	7.36449(9)
1173	3.16343(7)	9.96796(14)	7.36606(9)

Values from previous studies (ambient temperature)

H. & F.	3.144(3)	9.865(4)	7.297(3)
McD. & S.	3.145	9.857	7.296
R. & B.	3.14(5)	9.85(5)	7.29(3)

H. & F. = Hirose & Fujita (2005)

McD. & S. = McDaniel and Schneider (1972)

R. & B. = Rodi and Babel (1965)

Table 2: Linear and volumetric thermal expansion parameters for CaIrO_3 (for details see text; to reduce the effect of rounding errors in any subsequent calculations using these coefficients the values are sometimes reported to one more significant figure than is justified by their standard uncertainty).

	Value at T_r (300 K)	a_0	a_1
V	$226.402(7) \text{ \AA}^3$	$2.416(28) \times 10^{-5} \text{ K}^{-1}$	$7.30(39) \times 10^{-9} \text{ K}^{-2}$
a -axis	$3.14554(5) \text{ \AA}$	$0.453(14) \times 10^{-5} \text{ K}^{-1}$	$2.80(18) \times 10^{-9} \text{ K}^{-2}$
b -axis	$9.86370(8) \text{ \AA}$	$1.143(7) \times 10^{-5} \text{ K}^{-1}$	$0.86(10) \times 10^{-9} \text{ K}^{-2}$
c -axis	$7.29697(10) \text{ \AA}$	$0.829(12) \times 10^{-5} \text{ K}^{-1}$	$3.52(17) \times 10^{-9} \text{ K}^{-2}$

Table 3: CaIrO₃; fitted parameters for the second-order Grüneisen approximations (for details see text).

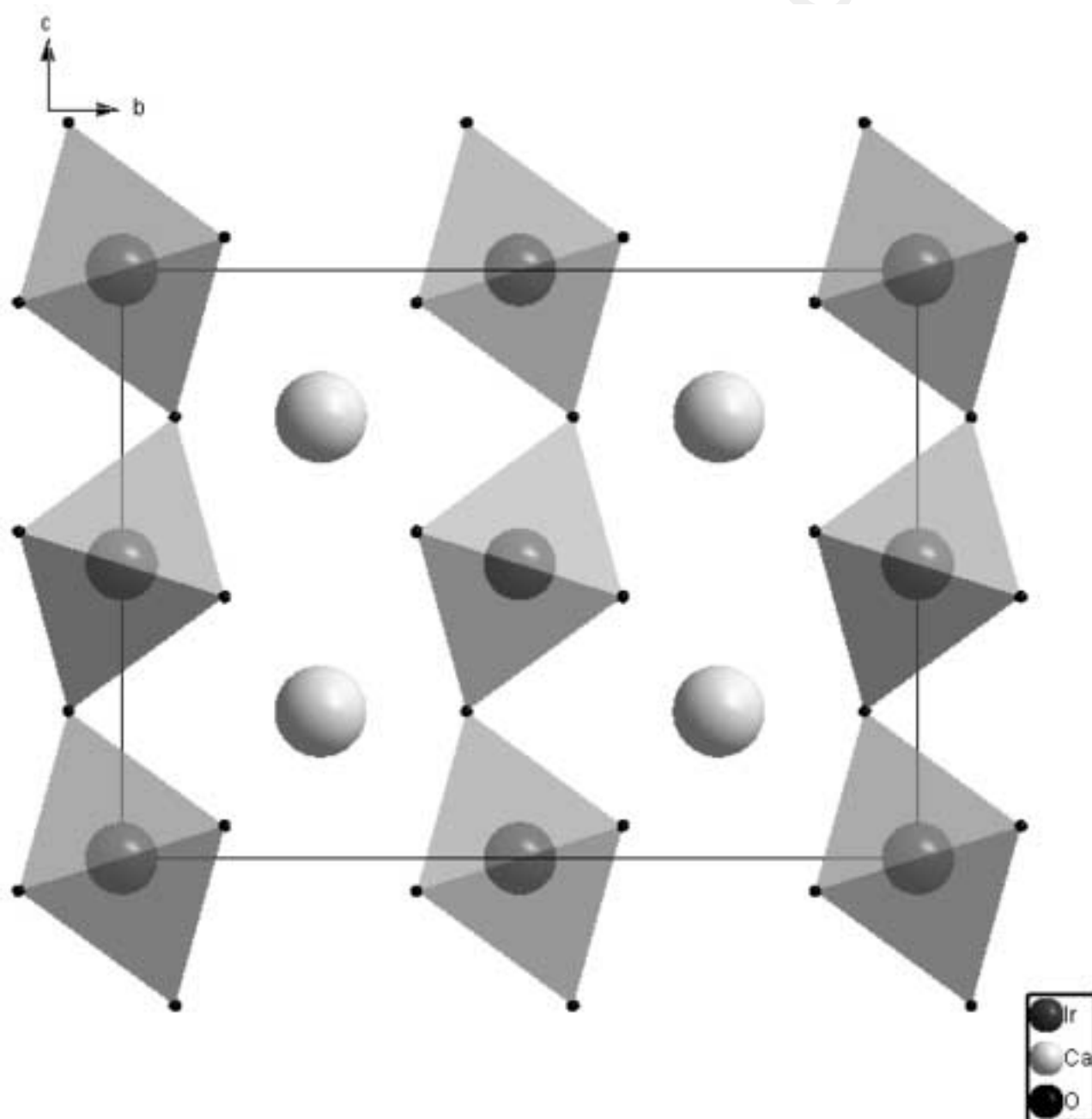
	q_D	Q	V_0	b
V	703(11) K	$2.77(2) \times 10^{-17}$ J	$225.666(6) \text{ \AA}^3$	1.9(2)
		Q_A	a_0	b_A
a -axis	648(37) K	$13.7(3) \times 10^{-17}$ J	$3.14317(7) \text{ \AA}$	21(3)
			b_0	
b -axis	647(15) K	$6.31(6) \times 10^{-17}$ J	$9.8485(2) \text{ \AA}$	-2.1(6)
			c_0	
c -axis	859(13) K	$7.30(7) \times 10^{-17}$ J	$7.29006(8) \text{ \AA}$	4.3(6)

Table 4: Axial Incompressibility ratios

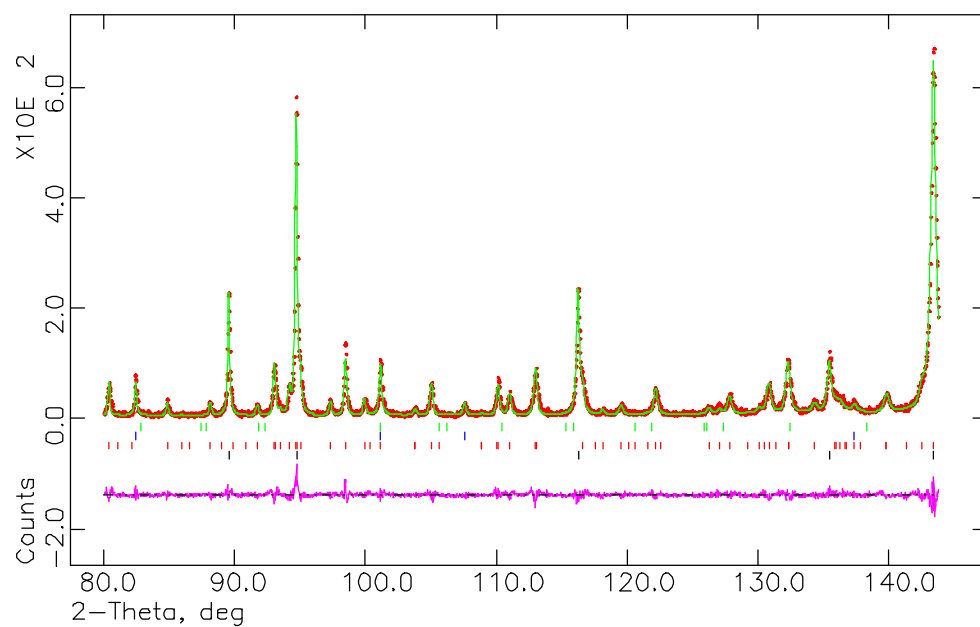
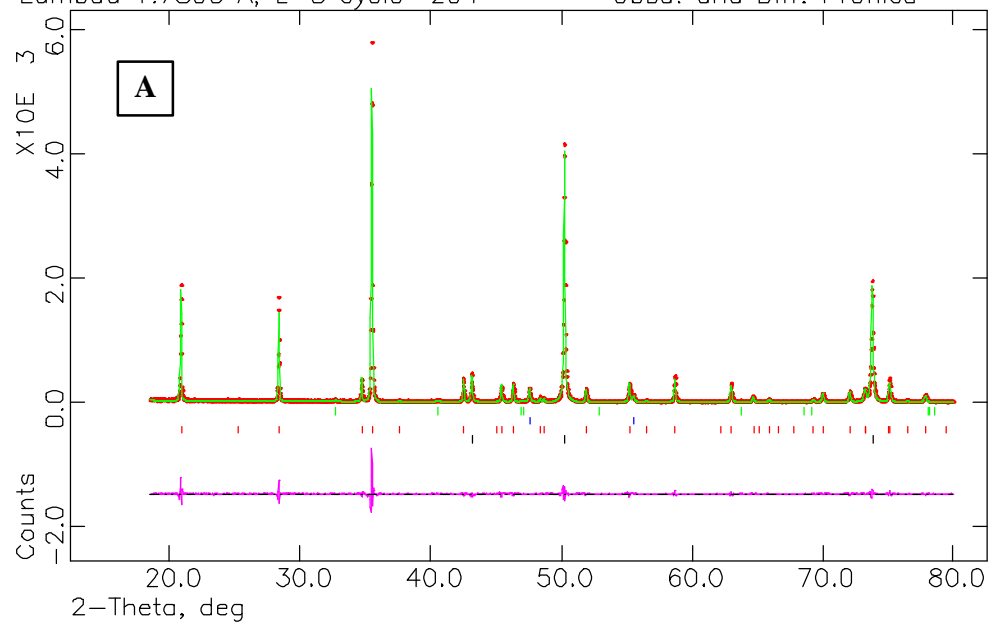
	a	:	b	:	c
CaIrO ₃ *	1.88		0.86		1
MgSiO ₃ : 136 GPa, 0 K	0.92		0.69		1
MgSiO ₃ : 136 GPa, 4000 K	0.95		0.71		1
Al ₂ O ₃ : 136 GPa, 0 K	1.09		0.97		1
Al ₂ O ₃ : 136 GPa, 4000 K	1.04		0.76		1

* Present Work

Remaining values taken from Stackhouse *et al.* (2005a,b)



MgO + CalrO3 in HTK 1200N – XU214–25 (XU213) Hist 2
Lambda 1.7890 Å, L–S cycle 294 Obsd. and Diff. Profiles



MgO + CalrO3 in HTK 1200N - XU214-900 Hist 3
 Lambda 1.7890 A, L-S cycle 291 Obsd. and Diff. Profiles

